

1 **Evaluation of rare earth on Layered Silicates under Subcritical**
2 **Conditions: Effect of the Framework and Interlayer Space**
3 **Composition**

4 **Pablo Chain¹, Agustín Cota^{1,2}, Said El Mrabet¹, Esperanza Pavón³, M. Carolina**
5 **Pazos¹, María D. Alba^{1*}**

6
7 ¹Instituto Ciencia de los Materiales de Sevilla- Departamento de Química Inorgánica, CSIC-
8 Universidad de Sevilla. Avda. Américo Vespucio, 49. 41092-Sevilla (Spain)

9 ²Laboratorio de Rayos-X. Centro de Investigación, Tecnología e Investigación de la Universidad de
10 Sevilla (CITIUS). Avda. Reina Mercedes, 4b. 41012-Sevilla (Spain)

11 ³Unité de Catalyse et de Chimie du Solide, UCCS, CNRS, UMR8181, Université Lille Nord de
12 France, 59655 Villeneuve d'Ascq (FRANCE)

13
14 **Abstract**

15 Clay-based minerals are considered to be an important component in backfill
16 barriers due to both their ability to seal and adsorb radioactive waste and to interact
17 chemically with it under subcritical conditions. Herein, we describe a systematic study of
18 the properties of layered silicates that could affect their hydrothermal reactivity, namely
19 type of layers, octahedral occupancy, origin and total amount of the layer charge, and
20 nature of the interlayer cation. The silicates studied were selected on the basis of their
21 different characteristics associated with these properties and were treated hydrothermally at
22 300°C for 48 h in a $7.3 \cdot 10^{-2}$ M $\text{Lu}(\text{NO}_3)_3 \cdot 3.6\text{H}_2\text{O}$ solution. The final products were
23 analyzed by X-ray diffraction and solid-state NMR spectroscopy. All the layered silicates
24 studied were found to be able to generate a $\text{Lu}_2\text{Si}_2\text{O}_7$ phase after hydrothermal treatment

* e-mail address of the corresponding author: alba@icmse.csic.es

25 under subcritical conditions, thereby confirming the participation of a chemical mechanism
26 of the clay barrier generating phases being stables with temperature and pH conditions.
27 However, the extent of this reaction depends to a large extent on the physicochemical
28 properties of the framework and the interlayer space composition, such as the presence or
29 absence of an octahedral sheet, the degree of occupancy of this sheet, and the origin and
30 total layer charge. Therefore, this study allows tuning the clay mineral framework
31 characteristic that favors the rare earth cations (as trivalent actinide simulator)
32 immobilization.

33

34 **Key Words**—Bentonite, smectite, Engineered barrier, disilicates, rare-earth, hydrothermal
35 treatment, subcritical conditions, X-ray diffraction, MAS-NMR, radioactive waste.

36

37 **1. Introduction**

38 High-level actinide-containing radioactive waste has become a key environmental
39 problem with the development of nuclear energy as a safe and efficient approach for long-
40 term waste storage must be found. A deep geological repository (DGR) based on an
41 engineered and natural multibarrier system is considered to be the most promising method
42 for the management of long-lived nuclear waste (Savage and Chapman., 1982). However,
43 the radionuclides stored in a DGR may reach the geosphere and the biosphere in the long-
44 term as a result of groundwater-induced dissolution of the canister and subsequent upward
45 transport by the water through the barriers and host rock. The most efficient way to enhance
46 radionuclide retention by sorption involves the construction of engineered barriers, which
47 are usually composed of clays (Meunier et al., 1998). Within the DGR, clay-engineered
48 barriers, which are usually placed between the metal canister containing the radioactive

49 waste and external concrete barriers, play a major role in radionuclide retention. The clay
50 minerals used tend to have low permeability and diffusivity, a high sorption capacity, and
51 strong buffering properties (Meunier et al., 1998; Landais, 2006; Itakura et al., 2010).
52 Smectites (the main constituent of the bentonites) are generally considered to be the most
53 efficient of the clays used for this purpose due to their ability to undergo strain without
54 fracturing, their low hydraulic conductivity, high cation sorption capacity, and their ability
55 to expand and enter into close contact with both waste and rock (Pusch, 2006). However,
56 both the physical and chemical nature of smectites is a key issue in the design of these
57 barriers as factors related to their microstructure and chemical properties, such as clay
58 geometry and isomorphic substitutions, may affect radionuclide sorption (Galunin et al.,
59 2010).

60 Groundwater infiltration, which can transport the radionuclides in dissolved form or
61 as colloids or small particles, is one of the main handicaps to be overcome during the
62 design and construction of safe nuclear waste repositories. Thus, if the water reaches the
63 canister and corrodes it, the barrier system should be able to retain the radionuclides in the
64 water and avoid their transport away from the repository (Cuadros, 2008). Interaction of
65 this barrier material with groundwater can, however, modify its physical and chemical
66 properties, thus decreasing its groundwater isolation capacity or, in the case of canister
67 failure, decreasing the radionuclide retention capacity of clay materials (Pusch et al., 2007).
68 Loss of the swelling and the cationic-exchange capacity of these materials under DGR
69 conditions has been well studied (Jennings and Thompson, 1986; Eberl et al., 1993;
70 Cuadros and Linares, 1996) and is recognized to be the main drawback to the use of
71 bentonite in DGRs (Meunier et al., 1998; Bauer et al., 2001). In light of this, an alternative
72 and effective immobilization mechanism could involve the chemical retention of actinides

73 by bentonite. This assumption is supported by studies of Perdigón (2002) and Alba and
74 Chaín (2005, 2007), who demonstrated that lutetium disilicate ($\text{Lu}_2\text{Si}_2\text{O}_7$) forms when a
75 nitric acid solution of lutetium reacts with saponite under pressures and temperatures
76 similar to those found in a DGR, even after weathering of the smectite. Moreover, the
77 persistence of $\text{Lu}_2\text{Si}_2\text{O}_7$ under hydrothermal conditions covering a wide range of pH and
78 different salt solutions has been demonstrated (Alba and Chain, 2007). Disilicate-phase
79 synthesis has therefore been proposed to be a possible long-term retention solution for
80 trivalent actinide cations.

81 To ensure optimal trivalent radioactive cation immobilization by chemical
82 interaction, it is important to understand the structural properties of smectites that enhance
83 their reactivity with Ln^{3+} ions and lead to formation of the disilicate phase. This
84 information could be extremely useful in finding smectites that yield the disilicate phase
85 under even milder conditions than those already reported, and would be especially relevant
86 to the design of effective repositories for high-level radioactive waste.

87 The main aim of this paper is to characterize the formation of $\text{Lu}_2\text{Si}_2\text{O}_7$ from a set of
88 different phyllosilicates upon treatment with a Lu^{3+} solution under subcritical conditions
89 and to establish the chemical and structural characteristics of these phyllosilicates that favor
90 this chemical reaction. Although Lu^{3+} is not the best lanthanide mimic of the trivalent
91 actinides most commonly found in high activity radioactive waste (Np, Am, and Cm)
92 (Astudillo, 2001), it is has been chosen because Alba et al. (2009) have shown that the
93 formation of rare-earth disilicates is common to all rare earths, with lutetium being the most
94 reactive.

95

96

97 2. Materials and methods

98

99 2.1. Materials

100

101 One of the seven well-characterized phyllosilicates selected for this study (structural
102 formulae are shown in Table 1) was a 1:0 phyllosilicate (with only a tetrahedral sheet, T),
103 whereas the remainder had a 2:1 layer structure (T-O-T structure). The 1:0 phyllosilicate
104 selected was a synthetic kanemite, $\text{Na}[\text{Si}_2\text{O}_4(\text{OH})]\cdot 3\text{H}_2\text{O}$, which is a layered silicate
105 containing only one sheet of orthosilicate tetrahedra. The orthosilicate groups are
106 condensed into three of its vertices (Q^3) in an irregular hexagonal arrangement. The silicate
107 sheets are bound by hydrogen bonds, and hydrated Na^+ cations that interact strongly with
108 the hydroxyl groups of the sheets are found in the interlayer space. A more detailed
109 structural description of this silicate can be found elsewhere (Alba et al., 2006). The
110 selected 2:1 phyllosilicates include a dioctahedral and a trioctahedral layered silicate, which
111 are almost free of no substitutional charge (pyrophyllite and talc respectively), three
112 trioctahedral smectites (saponite, hectorite, and Laponite[®]), and one trioctahedral
113 vermiculite, namely eucatex (Williams-Daryn et al., 2002). Two of these silicates
114 (vermiculite and saponite) contain Al substituting for Si in the tetrahedral sheet of the clay,
115 whereas the rest contain only Si in the tetrahedral sheet. Hectorite and Laponite[®] contain Li
116 substituting for Mg in the octahedral sheet and differ in their degree of crystallization,
117 which is poorer in Laponite[®] than in hectorite. Original samples with particle diameters of
118 less than 2 μm were used after removal of carbonates and organic matter.

119 Finally, a Na-hectorite was prepared by ion-exchange according to the method
120 described by Miller et al. (1982).

121

122 2.2. *Hydrothermal treatments*

123

124 A 300 mg sample of the powdered silicate and 50 mL of $7.3 \cdot 10^{-2}$ M
125 $\text{Lu}(\text{NO}_3)_3 \cdot 3.6\text{H}_2\text{O}$ solution were transferred into a stainless steel T316SS hydrothermal
126 reactor and heated to 300° C for 48 hours under autogenous pressure. After this time the
127 reactor was cooled to room temperature and the solids separated by filtration, washed
128 repeatedly with distilled water, and allowed to dry in air at 25°C. Although geochemical
129 waste degradation and waste/rock interaction processes in the hydrothermal environment
130 remain predictable up to temperatures of to about 200° C, many studies devoted to
131 simulating deep geological disposal conditions use temperatures of up to 350° C to increase
132 the reaction rates (Mather et al., 1982; Savage and Chapman, 1982; Allen and Wood, 1988;
133 Alba and Chain, 2007). The low solid/liquid ratio has been used in accordance with
134 previous related works (Alba and Chain, 2005; Alba et al., 2009; Galunin et al., 2009;
135 2010; 2011) and to allow performing the comparison of the results.

136

137 2.3. *Characterization*

138 2.3.1. *X-ray powder diffraction (XRD).*

139 XRD patterns were obtained using a Bruker D8I instrument at CITIUS (Centre of
140 Research, Technology and Innovation of Seville University), University of Seville (Spain).
141 This diffractometer works with a Ni-filtered Cu K_α radiation, at 40 kV and 40 mA.
142 Diffractograms were obtained from 3 to 70° 2 θ at a scan step of 0.05° 2 θ and with a
143 counting time of 3 s.

144

145 2.3.2. *NMR spectroscopy (MAS NMR).*

146 ^{29}Si , ^{27}Al , and ^1H single-pulse spectra were recorded using a Bruker DRX400
147 spectrometer with a magnetic field of 9.36 T and equipped with a multinuclear probe by the
148 Spectroscopy Service at ICMS (Material Science of Seville, CSIC-US). Powdered samples
149 were packed in 4 mm zirconia rotors and spun at 12 kHz. ^1H MAS NMR spectra were
150 obtained at a frequency of 400.13 MHz using a typical $\pi/2$ pulse width of 4.5 μs and a delay
151 time of 5 s. ^{29}Si MAS NMR spectra were obtained at a frequency of 79.49 MHz using a
152 pulse width of 2.7 μs ($\pi/2$ pulse length = 8.1 μs) and a delay time between 60 and 600 s.
153 ^{27}Al MAS NMR spectra were recorded at 104.26 MHz with a pulse width of 1.1 μs ($\pi/2$
154 pulse length = 11.0 μs) and delay time of 3 s. Chemical shifts are reported in ppm with
155 respect to tetramethylsilane for ^{29}Si and ^1H and a 0.1 M solution of AlCl_3 for ^{27}Al . All
156 spectra were simulated using a modified version of the Bruker Winfit program to handle the
157 finite spinning speed in MAS experiments (Massiot et al., 2002). A Gaussian–Lorentzian
158 model was used for all peaks. The fitted parameters were intensity, position, line-width, and
159 Gaussian/Lorentzian ratio.

160

161

162 **3. Results**

163 *3.1. Phyllosilicates with no substitutional charge*

164

165 The XRD pattern of kanemite (Fig. 1a) consisted of a set of reflections
166 corresponding to those of the standard kanemite structure PDF 25-1309 with a *020* basal
167 spacing of 10.2 Å (Johan and Maglione, 1972). All these reflections disappeared after
168 hydrothermal treatment in Lu^{3+} solution (Fig. 1b) to give a pattern similar to that of

169 $\text{Lu}_2\text{Si}_2\text{O}_7$ (PDF 35-0326) with small reflections corresponding to the secondary phases
170 tridymite (PDF 18-1170) and $\text{H}_2\text{Si}_2\text{O}_5$ (PDF 74-1548).

171 The XRD pattern of pyrophyllite (Fig. 1a) was indexed according to the PDF 46-
172 1308 pattern, with a basal spacing of 9.1 Å. Hydrothermal treatment in Lu^{3+} solution (Fig.
173 1b) did not alter the structure, crystallinity, or the collapsed state of the layers, which
174 maintained the basal spacing of the starting material. The emergence of a new reflection at
175 $14.6^\circ 2\theta$ was observed in the XRD pattern corresponding to boehmite (PDF 76-1871),
176 which was previously observed as a product of hydrothermal treatment of pyrophyllite
177 under aqueous acidic conditions at 300°C (Alba et al., 2010), thus indicating that this
178 structure shows some stability under hydrothermal conditions (Bentabol et al., 2003). The
179 whole set of reflections for the $\text{Lu}_2\text{Si}_2\text{O}_7$ phase was also evident alongside some minor
180 reflections for the $\text{H}_2\text{Si}_2\text{O}_5$ phase.

181 The XRD pattern of talc (Fig. 1a) was indexed according to PDF 29-1494, with a
182 basal spacing of 9.2 Å due to the non-swelling layered silicate. The presence of talc in the
183 XRD pattern of the treated sample (Fig. 1b) was minor, with the diffractogram being
184 dominated by the $\text{Lu}_2\text{Si}_2\text{O}_7$ phase. No other secondary phases arising from the
185 decomposition of talc were detected.

186 Analysis of the samples by MAS NMR spectroscopy was carried out to determine
187 the presence of any change in short-range order. The ^{29}Si MAS NMR spectra of the starting
188 materials and those obtained after hydrothermal treatment (Fig. 2, Table 2) revealed a
189 typical single signal centered at -97.3 ppm for kanemite due to the existence of Q^3 silicon
190 tetrahedra (Blasco et al., 1995). The spectra for treated samples show three signals at -91.8,
191 -100.5, and -111.5 ppm. The absence of a signal at -97.3 ppm indicates the absence of a Si
192 environment typical of kanemite. The most intense signal at -111.5 ppm was assigned to

193 the Q⁴(0Al) environment of tridymite, which presents a set of signals between -109.0 and -
194 113.0 ppm with a maximum at -111.0 ppm (Engelhardt and Michel, 1987). The signal at -
195 91.8 ppm corresponds to the Q¹ environment of Lu₂Si₂O₇ (Alba et al., 2001a; 2001b) and
196 implies a transformation of 11.4% of kanemite to this phase. Finally, the minor contribution
197 at -100.5 ppm was assigned to H₂Si₂O₅ (Heidemann et al., 1985). This finding is in good
198 agreement with the XRD data. The transformation of kanemite after hydrothermal reaction
199 was also evident in the ¹H MAS NMR spectra (Fig. 2 right). Thus, the ¹H MAS NMR
200 spectrum of the initial sample contains two broad signals, one at 4.80 ppm, which was
201 assigned to hydroxyl groups and free interlayer water, and the other at 14.80 ppm due to
202 water involved in the bridging hydrogen bonds (Alba et al., 2006). Only a narrow signal at
203 4.70 ppm, which could be assigned to hydration water of the Lu₂Si₂O₇ and H₂Si₂O₅ phases,
204 was observed after the hydrothermal treatment (Perdigón, 2002).

205 The ²⁹Si NMR spectrum of pyrophyllite (Fig. 2, Table 2) shows a signal at -95.2
206 ppm corresponding to a Q³ coordination sphere with no Al atoms in the neighboring
207 tetrahedra (Q³(0Al); Engelhardt and Michel, 1987). The spectra recorded after
208 hydrothermal treatment show a contribution in the same position as for the untreated
209 sample, along with two minor contributions due to Lu₂Si₂O₇ and H₂Si₂O₅ in a proportion of
210 4.3 % and 1.8 %, respectively. The ¹H MAS NMR spectra of untreated and treated
211 pyrophyllite show a single signal at 2.19 ppm, as could be expected for the ¹H resonance
212 signal of the hydroxyl group in dioctahedral 2:1 phyllosilicates (Alba et al., 2003). The ²⁷Al
213 MAS NMR spectra (not shown) of the untreated pyrophyllite (the only sample with
214 framework Al) and that recorded after the hydrothermal treatment were found to be
215 identical, with a single peak at ~0 ppm due to the octahedral Al environments (Engelhardt
216 and Michel, 1987). These results again suggest the stability of the pyrophyllite structure

217 after treatment. The formation of boehmite upon treatment of pyrophyllite produced no
218 spectral changes due to the octahedral coordination of Al in this phase (Engelhardt and
219 Michel, 1987).

220 Finally, talc showed a single contribution in the ^{29}Si MAS NMR spectrum at -98.1
221 ppm due to $\text{Q}^3(0\text{Al})$ (Sanz and Serratosa, 1984). The main peak (-91.7 ppm) in the
222 spectrum of the hydrothermally treated sample (83.6%) corresponds to the Q^1 environment
223 of $\text{Lu}_2\text{Si}_2\text{O}_7$. The remaining talc ^{29}Si signal at -97.7 ppm was found to be shifted towards
224 higher frequency (higher ppm value) upon hydrothermal treatment, possibly as a result of
225 vacancies in the octahedral sheet generated by Mg^{2+} leaching (Luce and Park, 1972; Sanz
226 and Serratosa, 1984; Corma et al., 1987). Mg^{2+} leaching from the octahedral sheet during
227 treatment was also evident from the shift of the hydroxyl ^1H NMR signal (Fig. 2b, right)
228 towards higher frequency (Alba et al., 2003). The ^1H MAS NMR spectrum of the treated
229 talc also shows a signal at 4.74 ppm due to hydration water of the $\text{Lu}_2\text{Si}_2\text{O}_7$ phase
230 (Perdigón, 2002).

231

232 *3.2. Charged phyllosilicates*

233

234 Structural changes in the long-range order of the charged trioctahedral 2:1
235 phyllosilicates after hydrothermal treatment were analyzed by XRD (Fig. 3 and 4). All the
236 reflections observed for the initial samples (Fig. 3a and 4a) were consistent with the general
237 and basal reflections of smectite and vermiculite, except the reflection at around $30^\circ 2\theta$ in
238 hectorite, which corresponds to cristobalite (PDF 03-272). The 060 reflections were
239 observed at a 2θ angle that corresponds to a distance of 1.51-1.53 Å between the reflection
240 planes, which is typical of trioctahedral 2:1 phyllosilicates (Grim, 1968). The 001 basal

241 reflection corresponds to a d_{00l} value of around 12.0 Å and was assigned to a water
242 monolayer around the interlayer cations (Alba et al., 2001a). The XRD pattern of Laponite®
243 showed broader reflections than the other silicates, mainly due to its smaller particle size,
244 which causes a relative loss of long-range order, and probably due to a mixed hydration
245 state (Wheeler et al., 2005).

246 In general, a complete absence of hkl reflections (Fig. 3b and 4b) is observed after
247 the hydrothermal treatment, thus indicating disruption of the basic structure of the silicates.
248 Indeed, except for vermiculite, hydrothermal treatment caused a partial swelling of the
249 layers due to the total replacement of the original interlayer cations by the trivalent cation
250 Lu^{3+} (Alba et al., 2001a). The number and intensity of the basal reflections decreased,
251 probably because of a lower-order stacking of the layers after treatment.

252 The emergence of small reflections corresponding to $\text{Lu}_2\text{Si}_2\text{O}_7$ was evident in both
253 hectorites (natural and homoionized in Na^+) after hydrothermal treatment (Fig. 3b). The
254 XRD pattern of the treated Na-hectorite was dominated by the crystalline phases of β -
255 cristobalite (PDF 89-3607) and enstatite (PDF 73-1937), which were accompanied by
256 minor reflections due to $\text{H}_2\text{Si}_2\text{O}_5$. No crystalline secondary phases were observed in the
257 XRD pattern of the treated hectorite, which only exhibited a broad signal in the range 20–
258 35° 2 θ due to the amorphous phase. The XRD pattern of treated Laponite® (Fig. 3b) only
259 showed reflections due to $\text{Lu}_2\text{Si}_2\text{O}_7$.

260 The XRD patterns of the treated saponite and vermiculite (Fig. 4b) were dominated
261 by $\text{Lu}_2\text{Si}_2\text{O}_7$, although other minor phases were also observed. Natrosilite (PDF 23-0529)
262 and $\text{H}(\text{Mg}_2(\text{SiO}_4))_8$ (PDF 87-2051) were formed in both samples, and kaolinite (PDF 78-
263 1996) and $\text{Mg}_{10}(\text{Si}_3\text{O}_{14})(\text{OH})_4$ (PDF 81-544) were also observed in vermiculite.

264 The changes in short-range order produced by the hydrothermal treatment were
265 followed by MAS NMR spectroscopic analysis of the active nuclei present in each silicate
266 (Fig. 5–7 and Tables 3 and 4). The only major signal in the ^{29}Si MAS NMR spectrum of
267 untreated hectorites (Table 3) was a peak in the range of chemical shifts associated with the
268 Q^3 (0Al) environment at -95.0 ppm. The shift of this signal to higher frequencies with
269 respect to talc is due to the isomorphic substitution of Li^+ for Mg^{2+} in the octahedral sheet,
270 which resulted in a decrease in the electronegativity of the cations coordinated by the apical
271 oxygen of the tetrahedral sheet (Weiss et al., 1987). Hydrothermal treatment resulted in
272 more complex ^{29}Si MAS NMR spectra for both hectorites. These spectra were
273 deconvoluted into six contributions (see Table 3). The signals for both these samples
274 corresponded to similar environments but with different relative intensities. The main
275 differences can be summarized as follows: (i) the Q^3 (0Al) signal of the remaining hectorite
276 was 27.1% in the natural hectorite and 5.8% in the Na-hectorite; (ii) the Q^1 environment of
277 $\text{Lu}_2\text{Si}_2\text{O}_7$ (-91.7 ppm) was 13.3% and 12.7%, respectively; (iii) a signal at -79.8 ppm
278 assigned to the Q^0 environment of $\text{X}_2\text{-Lu}_2\text{SiO}_5$ (16.4%; Becerro et al., 2004), which was
279 absent in the Na-hectorite, was observed in the natural sample; and (iv) the other signals at
280 around -85 ppm, -101 ppm, and -111 ppm corresponded to the secondary phases enstatite
281 (Mägi et al., 1984), H_2SiO_5 (Heidemann et al., 1985) and β -cristobalite (Smith and
282 Blackwell, 1983), which together contributed a total of 43.2% and 81.5%, respectively.

283 The initial spectrum of Laponite[®] (Table 3) was characterized by a main signal at -
284 94.5 ppm, which was assigned to a Q^3 (0Al) environment, along with a shoulder at -97.3
285 ppm and a minor peak at -85.2 ppm. The main signal shifted to higher frequency with
286 respect to that for hectorite due to the increased layer-charge deficit in Laponite[®] (Weiss et
287 al., 1987). The signal at -97.3 ppm was due to the presence of partially condensed Si

288 tetrahedra with anionic basal oxygens, in other words $(\text{SiO})_3\text{SiO}^-$ (Wheeler et al., 2005),
289 whereas the higher-frequency signal was assigned to silanol groups, namely $(\text{SiO})_3\text{SiOH}$
290 (Weiss et al., 1987; Wheeler et al., 2005). The signals of the original spectrum disappeared
291 after hydrothermal treatment and two new signals, corresponding to $\delta\text{-Na}_2\text{Si}_2\text{O}_5$ (Mortuza,
292 1989) and $\text{Lu}_2\text{Si}_2\text{O}_7$, appeared at -90.6 ppm (27.2%) and -91.7 ppm (72.8%), respectively.

293 The ^{29}Si MAS NMR spectrum of the untreated saponite showed a signal with three
294 contributions (Table 4): an intense signal at -95.8 ppm and two lower-intensity signals at -
295 90.8 and -85.0 ppm, corresponding to $\text{Q}^3(0\text{Al})$, $\text{Q}^3(1\text{Al})$, and $\text{Q}^3(2\text{Al})$ Si environments,
296 respectively (Alba et al., 2001b). Calculation of the Si/Al ratio gave a value of 8.4, which
297 agrees well with the theoretical value of 9.0 obtained from the chemical formula. The
298 treated sample exhibited a ^{29}Si MAS NMR spectrum containing four signals. The
299 remaining saponite showed only a single ^{29}Si contribution at -95.0 ppm (2.4%) due to the
300 $\text{Q}^3(0\text{Al})$ Si environment, thus indicating that hydrothermal treatment results in the absence
301 of $\text{Q}^3(1\text{Al})$ and $\text{Q}^3(2\text{Al})$ Si environments, possibly due to partial leaching of Al from the
302 tetrahedral sheet. The other three new signals are found at -91.7, -88.5, and -72.5 ppm and
303 correspond to $\text{Lu}_2\text{Si}_2\text{O}_7$ (71.4%), natrosilite (Alba and Chain, 2005), and the Q^1 Si
304 environments of $\text{H}(\text{Mg}_2(\text{SiO}_4))_8$ (Engelhardt and Michel, 1987; Haiber et al., 1997).

305 The ^{29}Si NMR signals obtained for vermiculite (Table 4) were abnormally broad
306 due to the presence of Fe in its structure. Thus, the single signal with a maximum at -88.5
307 ppm, due to Q^3 environments, observed for the untreated sample could be fitted to four
308 peaks (Table 4). The small Si/Al ratio in this silicate (3.5) resulted in a greater contribution
309 of $\text{Q}^3(m\text{Al})$ with $m \neq 0$ environments to the ^{29}Si signal than in the saponite sample. The
310 signals corresponding to the vermiculite disappeared after hydrothermal treatment and the
311 ^{29}Si MAS NMR spectrum was composed of three new signals at -91.4, -88.2, and -76.3

312 ppm, which were assigned to $\text{Lu}_2\text{Si}_2\text{O}_7$ (57.9%), natrosilite, and the Q^1 and Q^0 Si
313 environments of the magnesium silicate phases (Pacalo and Parise, 1992; Haiber et al.,
314 1997) observed by XRD.

315 The ^1H MAS NMR spectra of the untreated smectites (Fig. 5 and 6, right) showed
316 two well-resolved peaks, one in the range 0.30-0.65 ppm, which was assigned to
317 framework hydroxyl groups, and the other in the range 3.70-4.30 ppm, which was assigned
318 to interlayer water. The position of both signals was found to depend on the chemical
319 composition of the smectite (Alba et al., 2003). In general, hydrothermal treatment resulted
320 in a shift of the hydroxyl signal to greater frequency, as observed previously when
321 vacancies in the octahedral sheet were produced by leaching of framework cations (Alba et
322 al., 2003). This treatment also caused the water signal to shift to higher frequency due to
323 replacement of the Na^+ or Ca^{2+} interlayer cation by framework Mg^{2+} , Al^{3+} , or Lu^{3+} from the
324 solution (Alba et al., 2003). Moreover, the water signals were found to be broader after
325 treatment due to the miscellaneous composition of the interlayer space. The ^1H MAS NMR
326 spectra of the untreated and treated vermiculite did not allow the two expected proton
327 environments to be resolved due to the amount of paramagnetic impurities present in the
328 silicate, thus meaning that these spectra were of little analytical value.

329 A ^{27}Al MAS NMR study was only carried out for the aluminum silicates saponite
330 and vermiculite (Fig. 7), both of which showed a single signal at around 60 ppm due to
331 tetrahedral Al (Engelhardt and Michel, 1987). The hydrothermal treatment of both samples
332 resulted in the appearance of a new signal at around 0 ppm due to octahedral Al
333 (Engelhardt and Michel, 1987) and disappearance of the signal at around 60 ppm as a result
334 of Al leaching from the tetrahedral sheet. These findings are in good agreement with the

335 disappearance of the $Q^3(mAl)$ with $m \neq 0$ environments from the ^{29}Si MAS NMR spectra
336 after treatment.

337

338 **4. Discussion**

339 The XRD and NMR results show that the 1:0 and 2:1 phyllosilicates are chemically
340 suitable for $Lu_2Si_2O_7$ formation.

341 An analysis of the results for kanemite, pyrophyllite, and talc allow the role of the
342 octahedral layer in the generation of lutetium disilicate to be defined. Likewise, the order of
343 reactivity can be extracted from the contribution of the Q^1 Si environment ($Lu_2Si_2O_7$) to the
344 ^{29}Si MAS NMR spectra, with talc being the most reactive (83.6%), followed by kanemite
345 (11.4%), and, finally, pyrophyllite (4.3%). As can be seen from the XRD results, the higher
346 hydrothermal stability of trioctahedral silicates with respect to their dioctahedral
347 counterparts in neutral and acidic media (Alba et al., 2010) could favor the permanence of
348 the laminar structure before the reaction with lutetium, and thus a suitable environment for
349 generating the disilicate phase (Becerro et al., 2003). The laminar structure of the silicate
350 has been shown to be the main factor favoring disilicate phase generation, thus meaning
351 that the SiO_2 as a source of silicon is unable to produce disilicates under hydrothermal
352 conditions (Perdigón, 2002).

353 The results obtained for kanemite are more difficult to interpret as two competing
354 factors participate in the process. Thus, the absence of an octahedral sheet confers a high
355 flexibility to the layers, thereby allowing this material to be used as a precursor for the
356 synthesis of a large number of compounds (Kooli, 2002; Selvam et al., 2003) that could
357 evolve towards stable structures under hydrothermal conditions. However, this same

358 flexibility is accompanied by a low hydrothermal stability that results in the evolution of Q³
359 environments towards Q⁴ condensation and therefore lower reactivity (Perdigón, 2002).

360 The layer charge in 2:1 phyllosilicates results from isomorphic substitutions in the
361 tetrahedral or octahedral sheets. The influence of this layer charge can be determined by
362 comparing the reactivity of saponite and hectorite/Laponite®. Thus, saponite and
363 Laponite® present a higher reactivity as regards the formation of RE disilicate (71.4% and
364 72.8%, respectively), followed by hectorite (13.3%). The marked difference in reactivity
365 between saponite and hectorite in favor of the former is due to substitutions in the
366 tetrahedral sheet rather than in the octahedral layer (Alba et al., 2001a; 2001b). Thus, Li⁺
367 leaches more easily than Mg²⁺ from the octahedral sheet and the latter leaches more easily
368 than Al³⁺ from the tetrahedral sheet. This is evident upon comparing the XRD diffraction
369 patterns of hectorite and saponite, with the former being compatible with the presence of
370 most of the components as an amorphous phase, whereas the persistence of the 001
371 reflection in the saponite XRD pattern is compatible with the presence of hydrated Lu³⁺
372 and/or Al³⁺ in the interlayer space. The marked difference in reactivity between Laponite®
373 and hectorite, which have a similar origin and layer charge, is due to the smaller particle
374 size in Laponite® (Wheeler et al., 2005). This smaller particle size and the largest number
375 of structural defects improve the reaction kinetics since this reaction follows a
376 reconstructive reaction mechanism (Archilla et al., 2006).

377 The influence of the layer charge on the hydrothermal reactivity can be studied by
378 comparing the results obtained for saponite and the vermiculite eucatex, with the main
379 difference between the two being the higher layer charge of the vermiculite. The formation
380 of Lu₂Si₂O₇ is higher for saponite (71.4%) than for vermiculite (57.9%), thus apparently
381 contradicting the observed guideline whereby substitutions in the tetrahedral sheet increase

382 the reactivity. Therefore, the main responsible for this reactivity order may be the highest
383 hydrothermal stability of the saponite versus vermiculite, as previously reported by Alba et
384 al. (2010). A possible explanation for this finding is that an increase in the number of
385 substitutions in the tetrahedral sheet favors the leaching of Al^{3+} cations, which in turn leads
386 to disintegration of the structure to form a more stable and less reactive phase, like
387 kaolinite. This is also reinforced by the greater reactivity shown by talc, which is a neutral
388 trioctahedral layered silicate.

389 Finally, analysis of the effect of the interlayer cation on the synthesis is based on the
390 results obtained from hectorites (natural Ca-hectorite and homoionized with Na^+). Both
391 these materials display a similar hydrothermal reactivity as regards $Lu_2Si_2O_7$ formation (ca.
392 13%) but with an important difference in terms of hydrothermal stability in favor of the
393 natural hectorite (the remaining $Q^3(OAl)$ contribution was 27.1% and 5.8%, respectively).
394 The long-range order is lost in both cases, as observed by XRD. In addition, the degree of
395 crystallization of secondary products is more advanced in the Na-hectorite. Finally, the
396 presence of $X_2-Lu_2SiO_5$, which has previously been detected as a degradation product when
397 Ca is present in the reaction medium, was observed for the natural hectorite (Alba and
398 Chain, 2007).

399

400 **5. Conclusions**

401

402 All the layered silicates studied are able to generate a $Lu_2Si_2O_7$ phase after
403 hydrothermal treatment under subcritical conditions, thus demonstrating the additional
404 chemical immobilization mechanism of the clay barrier. However, the extent of this

405 reaction depends on the presence or absence of an octahedral sheet, the degree of
406 occupancy of this sheet, and the total layer charge and its origin.

407 In the context of engineered-barrier safety, the structure of the selected bentonite
408 must fulfill the following conditions: 2:1 layer stacking (T-O-T structure) with complete
409 occupancy of the octahedral sheet, the absence of octahedral isomorphous substitutions, and
410 a moderate tetrahedral isomorphous substitution of Al for Si. As a secondary factor, sodium
411 is preferred to calcium as an interlayer cation because the presence of calcium in the
412 medium favors the formation of the Lu_2SiO_5 vs $\text{Lu}_2\text{Si}_2\text{O}_7$, a most stable phase. These
413 requirements provide a higher hydrothermal reactivity.

414

415 **Acknowledgements**

416 We gratefully acknowledge financial support from DGICYT and FEDER funds (Projects CTQ2010-14874).

417 **References**

- 418 Alba, M.D., Becerro, A.I., Castro, M.A., Perdigón A.C, 2001a. Hydrothermal reactivity of Lu-saturated
419 smectites: Part I. A long-range order study. *American Mineralogist* 86, 115-123.
- 420 ——— 2001b. Hydrothermal reactivity of Lu-saturated smectites: Part II. A short-range order study.
421 *American Mineralogist* 86, 124-131.
- 422 Alba, M.D., Becerro, A.I., Castro, M.A., Perdigón, A.C., Trillo, J.M., 2003. Inherent acidity of aqua metal
423 ions in solids: assay in layered aluminosilicates. *Journal of Physical Chemistry B* 107, 3996-4001.
- 424 Alba, M.D., Castro, M.A., Chain, P., Orta, M.M, Pazos, M.C., Pavon, E., 2010. Hydrothermal stability of
425 layered silicates in neutral and acidic media: Effect on engineered-barrier safety. *Clays and Clay*
426 *Minerals* 4, 501-514.
- 427 Alba, M.D., Chain, P., 2005. Interaction between Lutetium Cations and 2:1 Aluminosilicates under
428 Hydrothermal Treatment. *Clays and Clay Minerals* 53, 39-46.

- 429 ——— 2007. Persistence of lutetium disilicate. *Applied Geochemistry* 22, 192-201.
- 430 Alba, M.D., Chain, P., Orta, M.M., 2009. Chemical reactivity of argillaceous material in engineered barrier
431 Rare earth disilicate formation under subcritical conditions. *Applied Clay Science* 43, 369-375.
- 432 Alba, M.D., Chain, P., Pavón E., 2006. Synthesis and characterization of gallium containing kanemite.
433 Microporous and Mesoporous Materials 94, 66-73.
- 434 Allen, C.C., Wood, M.I., 1988. Bentonite in Nuclear Waste Disposal: A Review of Research in Support of the
435 Basalt Waste Isolation Project. *Applied Clay Science* 3, 11-30.
- 436 Ames, L.L., Sand, L.B., Goldich, S.S., 1958. A contribution on the Hector, California bentonite deposit.
437 *Economic Geology* 53, 22-37.
- 438 Archilla, J.F.R., Cuevas, J., Alba, M.D., Naranjo, M., Trillo, J.M., 2006. Discrete breathers for understanding
439 reconstructive mineral processes at low temperature. *Journal of Physical Chemistry B* 110, 24112-
440 24120.
- 441 Astudillo, J., 2001. "El almacenamiento geológico profundo de los residuos radiactivos de alta actividad.
442 Principios básicos y tecnología.", Editorial ENRESA.
- 443 Bauer, A., Scafer, T., Dohrmann, R., Hoffmann, H., Kim, J.J., 2001. Smectite stability in acid salt solutions
444 and the fate of Eu, Th and U in solution. *Clay Mineral* 36, 93-103.
- 445 Becerro, A.I., Naranjo, M., Perdígón, A.C., Trillo, J.M., 2003. Hydrothermal chemistry of silicates: low-
446 temperature synthesis of γ -Yttrium disilicate. *Journal of American Ceramic Society* 86, 1592-1594.
- 447 Becerro, A.I., Escudero, A., Florian, P., Massiot, D., Alba, M.D., 2004. Revising $Y_2Si_2O_7$ and Y_2SiO_5
448 polymorphic structures by ^{89}Y MAS-NMR spectroscopy. *Journal of Solid State Chemistry* 177, 2783-
449 2789.
- 450 Bentabol, M., Cruz, M.D.R., Huerta, F.J., Linares, J., 2003. Hydrothermal transformation of kaolinite at 200
451 and 300 degrees C. *Clay Minerals* 38, 161-172.
- 452 Blasco, T., Corma, A., Navarro, M.T., Pariente, J.P., 1995. Synthesis, characterization, and catalytic activity
453 of Ti- MCM-41 structures. *Journal of Catalysis* 156, 65-74.
- 454 Corma, A., Mifsud, A., Sanz, E., 1987. Influence of the chemical composition and textural characteristic of
455 palygorskite on the acid leaching of octahedral cations. *Clay Minerals* 22, 225-232.
- 456 Cuadros, J., 2008. Clays as sealing material in nuclear waste repositories. *Geology Today* 24, 90-103.

457 Cuadros, J., Linares, J., 1996. Experimental Kinetic study of the smectite-illite transformation. *Geochimica et*
458 *Cosmochimica Acta*, 60, 439-453.

459 Eberl, D.D., Velde, B., McCormick, T., 1993. Synthesis of illite-smectite from smectite at earth surface
460 temperatures and high pH. *Clay Minerals* 28, 49-60.

461 Engelhardt, G., Michel, D. (editors), 1987. *High-resolution Solid-State NMR of Silicates and Zeolites*. John
462 Wiley & Sons, New York.

463 Galunin, E., Alba, M.D., Aviles, M.A., Santos, T., Vidal, M., 2009. Reversibility of la and Lu sorption onto
464 smectites: Implications for the design of engineered barriers in deep geological repositories. *Journal of*
465 *Hazardous Materials* 172, 1198-1205.

466 Galunin, E., Alba, M.D., Santos, M.J., Abrao, T., Vidal, M., 2010. Lanthanide sorption on smectitic clays in
467 presence of cement leachates. *Geochimica et Cosmochimica Acta* 74, 862-875.

468 Galunin, E., Alba, M.D., Santos, M.J., Abrao, T., Vidal, M., 2011. Examination of competitive lanthanide
469 sorption onto smectites and its significance in the management of radioactive waste. *Journal of*
470 *Hazardous Materials* 186, 1930-1941.

471 Grim, R.E., 1968. *Clay Mineralogy*: McGraw-Hill Book Company, New York.

472 Haiber, M., Ballone, P., Porinello, M., 1997. Structure and dynamics of protonated Mg_2SiO_4 : An ab-initio
473 molecular dynamics study. *American Mineralogist* 82, 913-922.

474 Heidemann, D., Grimmer, A.R., Hübert, C., Starke, P., Mägi, M., 1985. Solid-state high-resolution Si-29
475 NMR-studies of polycrystalline phyllosilicic acids $(H_2Si_2O_5)_x$ at low and high magnetic-field.
476 *Zeitschrift für Anorganische und Allgemeine Chemie* 528, 22-36.

477 Itakura, T., Airey, D.W., Leo, C.J., Payne, T., McOrist, G.D., 2010. Laboratory studies of the diffusive
478 transport of Cs-137 and Co-60 through potential waste repository soils. *Journal of Environmental*
479 *Radioactivity* 101, 723-729.

480 Jennings, S., Thompson, G.R., 1986. Diagenesis of Pilo-Pleistocene sediments of the Colorado River Delta,
481 southern California. *Journal of Sedimentary Petrology* 56, 89-98.

482 Johan, Z., Maglione, G.F., 1972. Kanemite a new hydrated sodium silicate. *Bulletin de la Société Française*
483 *Mineralogie et de Cristallographie* 95, 371-382.

484 Kooli, F., 2002. Recrystallization of a new layered silicate from Na-kanemite-tetramethylammonium
485 hydroxide-water-,4-dioxane mixture. *Journal of Materials Chemistry* 12, 1374-1380.

486 Landais, P., 2006. Advances in geochemical research for the underground disposal of high-level, long-lived
487 radioactive waste in a clay formation. *Journal of Geochemical Exploration* 88, 32-36.

488 Laporte Industries Ltd. (1990) Laponite Technological Bulletin, L104/90/A, 1.

489 Levitz, P., Lecolier, E., Mourchid, A., Delville, A., Lyonnard, S., 2000. Liquid-solid transition of laponite
490 suspension at very low ionic strength: Long-range electrostatic stabilization of anisotropic colloids.
491 *Europhysics Letters* 49, 672-677.

492 Luce, R.W, Parks, G.A., 1972. Dissolution kinetics of magnesium silicates. *Geochimica et Cosmochimica*
493 *Acta* 36, 35-50.

494 Mägi, M., Lippmaa, E., Samoson, A., 1984. Solid-State High-Resolution Si-29 Chemical-Shift in Silicates.
495 *Journal of Physical Chemistry* 88, 1518-1522.

496 Massiot, D., Fayon, F., Capron, M., King, I., Le Calvé, S., Alonso, B., Durand, J.O., Bujoli, B., Gan, Z.,
497 Hoatson, G., 2002. Modelling one- and two-dimensional solid-state NMR spectra. *Magnetic*
498 *Resonance in Chemistry* 40, 70-76.

499 Mather, J.D., Chapman, N.A., Black, J.H., Lintern, B.C., 1982. The geological disposal of high-level
500 radioactive waste-a review of the Institute of Geological Sciences Research programme. *Nuclear*
501 *Energy* 21, 167-173.

502 Meunier, A., Velde, B., Griffault, L., 1998. The reactivity of bentonites: a review. An application to clay
503 barrier stability for nuclear waste storage. *Clays and Clay Minerals* 33, 187-196.

504 Miller, S.E., Heath, G.R., González, R.D., 1982. Effects of Temperature on the Sorption of Lanthanides by
505 Montmorillonites. *Clays and Clay Minerals* 30, 111-122.

506 Mortuza, M.G., 1989. A Nuclear Magnetic Resonance Investigation of the Structure of Some Alkali Silicate
507 Glasses. PhD Thesis, University of Warwick.

508 Pacalo, R.E.G., Parise, J.B., 1992. Crystal-Structure of Superhydrous-B, a Hydrous Magnesium-Silicate
509 Synthesized at 1400-Degrees-C and 20-GPa. *American Mineralogist* 77, 681-684.

510 Perdigón, A.C., 2002. Estudio del sistema saponita/Lu(NO₃)₃/H₂O en condiciones hidrotérmicas. Ph.D.thesis,
511 University of Seville, Seville (Spain).

512 Petit, S., Martin, F., Wiewiora, A., De Parseval, P., Decarreau, A., 2004. Crystal-chemistry of talc: A near
513 infrared (NIR) spectroscopy study. *American Mineralogist* 89, 319-326.

514 Prost, J.L., 1984. Saponite from near ballarat, California. *Clays and Clay Minerals* 32, 147-153.

515 Pusch, R., 2006. Engineered Barriers, in: V. Popov, R. Pusch (Eds.), *Disposal of hazardous waste in*
516 *underground mines*, Wessex Institute of Technology, UK, pp. 35-40.

517 Pusch, R., Kasbohm, J., Pakovsky, J., Cechova, Z., 2007. Are all smectite clays suitable as “buffers”. *Physics*
518 *and Chemistry of the Earth* 32, 116–122.

519 Sánchez-Soto, P.J., Justo, A., Pérez-Rodríguez, J.L., 1994. Griding effect on kaolinite pyrophyllite illite
520 natural mixtures and its influence on mullite formation. *Journal of Materials Science* 29, 1276–1283.

521 Sanz, J., Serratosa, J.M., 1984. Si-29 and Al-27 High-Resolution MAS-NMR spectra of phyllosilicates.
522 *Journal of the American Chemical Society* 106, 4790-4793.

523 Savage, D., Chapman, N.A., 1982. Hydrothermal behaviour of simulated waste glass- and waste-rock
524 interaction under repository conditions. *Chemical Geology* 36, 59-86.

525 Selvam, T., Bandarapu, B., Mabande, G.T.P., Toufar, H., Schwieger, W., 2003. Hydrothermal transformation
526 of layered sodium silicate, kanemite, into zeolite beta (BEA). *Microporous and Mesoporous Materials*
527 64, 41-50.

528 Smith, J.V., Blackwell, C.S., 1983. Nuclear Magnetic-Resonance of Silica Polymorphs. *Nature* 303, 223-225.

529 Weiss, C.A., Altaner, S.P., Kirkpatrick, R.J., 1987. High resolution ²⁹Si NMR spectroscopy of 2:1 layer
530 silicates: Correlations among chemical shift, structural distortions, and chemical variations. *American*
531 *Mineralogist* 72, 935-942.

532 Wheeler, P.A., Wang, J., Baker, J., Mathias, L.J., 2005. Synthesis and characterization of covalently
533 functionalized Laponite clay. *Chemistry of Materials* 17, 3012-3018.

534 Williams-Daryn, S., Thomas, R.K., Castro, M.A., Becerro A., 2002. The structures of complexes of a
535 vermiculite intercalated by cationic surfactants, a mixture of cationic surfactants, and a mixture of
536 cationic and non-ionic surfactants. *Journal of Colloid and Interface Science* 256, 314-324.

537

Table 1. Layered aluminosilicates used as starting materials

Silicate	Source	Chemical Formulae
Kanemite ¹	Synthetic ^a	Na[Si ₂ O ₄ (OH)]·3H ₂ O
Pyrophyllite ²	Natural Hillsboro	(Ca _{0.006} Na _{0.012} K _{0.018})[Si ₄][Al _{1.95} Fe _{0.01} Ti _{0.005} Mg _{0.001}]O ₁₀ (OH) ₂
Talc ³	Natural Lillo	[Si ₄][Mg _{2.95} Fe _{0.017}]O ₁₀ F _{0.19} (OH) _{1.81}
Hectorite ⁴	Natural ^b S.Bernardino	Ca _{0.17} [Si _{3.98} Al _{0.02}][Mg _{2.65} Al _{0.02} Li _{0.33}]O ₁₀ (OH) ₂
Laponite® ⁵	Synthetic ^c	Na _{0.35} [Si ₄][Mg _{2.73} Li _{0.2}]O ₁₀ (OH) ₂
Saponite ⁶	Natural ^b California	Na _{0.31} K _{0.01} Ca _{0.04} [Si _{3.6} Al _{0.4}][Mg _{2.9} Fe _{0.07}]O ₁₀ (OH) ₂
Vermiculite ⁷	Natural Eucatex	Na _{0.7} [Si _{3.1} Al _{0.9}][Mg _{2.48} Al _{0.08} Fe _{0.31} Ti _{0.04} Mn _{0.01}]O ₁₀ (OH) ₂

(a) synthesized by Alba et al. (2006); (b) Source Clays Repository of the Clay Minerals Society, *University of Missouri, Columbia, USA*; (c) Solvay Alkali GMBH

(1) Alba et al., 2006 ; (2) Sánchez Soto et al., 1994; (3) Petit et al., 2004; (4) Laporte Industries Ltd, 1990; Levitz et al., 2000; (5) Prost, 1984; Alba et al., 2001a and 2001b; (6) Ames et al., 1958; (7) Williams-Daryn et al., 2002

538

539

540

Table 2. ^{29}Si chemical shift, FWHM and area under the curve of the different contributions obtained from the fitting of the ^{29}Si MAS NMR spectrum of kanemite, pyrophyllite and talc.

δ (ppm)	FWHM (Hz)	%	phase
kanemite			
<i>Starting material</i>			
-97.3±0.1	99±1	100	Q ³ (0Al)
<i>After hydrothermal treatment in a 7.3·10⁻² M Lu(NO₃)₃·3.6H₂O solution</i>			
-91.8±0.1	97±2	11.4	Lu ₂ Si ₂ O ₇
-100.5±0.2	134±37	0.9	H ₂ Si ₂ O ₅
-111.5±0.1	461±3	87.7	Q ⁴ (0Al)
pyrophyllite			
<i>Starting material</i>			
-95.2±0.1	111±1	100	Q ³ (0Al)
<i>After hydrothermal treatment in a 7.3·10⁻² M Lu(NO₃)₃·3.6H₂O solution</i>			
-92.1±0.1	161±11	4.3	Lu ₂ Si ₂ O ₇
-95.0±0.1	104±1	93.9	Q ³ (0Al)
-99.0±0.1	122±15	1.8	H ₂ Si ₂ O ₅
talc			
<i>Starting material</i>			
-98.1±0.1	141±1	100	Q ³ (0Al)
<i>After hydrothermal treatment in a 7.3·10⁻² M Lu(NO₃)₃·3.6H₂O solution</i>			
-91.7±0.1	126±1	83.6	Lu ₂ Si ₂ O ₇
-97.7±0.1	134±4	16.4	Q ³ (0Al)

Table 3. ^{29}Si chemical shift, FWHM and area under the curve of the different contributions obtained from the fitting of the ^{29}Si MAS NMR spectrum of hectorite, Na-hectorite and Laponite[®]

δ (ppm)	FWHM (Hz)	%	phase
hectorite			
<i>Starting material</i>			
-95.0±0.1	239±2	100	Q ³ (0Al)
<i>After hydrothermal treatment in a 7.3·10⁻² M Lu(NO₃)₃·3.6H₂O solution</i>			
-79.8±0.1	629±25	16.4	X ₂ -Lu ₂ SiO ₅
-86.4±0.1	687±43	27.4	enstatite
-91.4±0.1	261±15	13.3	Lu ₂ Si ₂ O ₇
-94.6±0.1	392±16	27.1	Q ³ (0Al)
-100.9±0.3	740±74	10.8	H ₂ Si ₂ O ₅
-110.2±0.1	390±28	5.0	crystalite
Na-hectorite			
<i>After hydrothermal treatment in a 7.3·10⁻² M Lu(NO₃)₃·3.6H₂O solution</i>			
-84.1±0.2	481±44	7.1	enstatite
-91.6±0.1	167±6	12.7	Lu ₂ Si ₂ O ₇
-95.3±0.1	215±28	5.8	Q ³ (0Al)
-100.7±0.3	667±65	14.4	H ₂ Si ₂ O ₅
-111.5±0.1	273±15	60.0	crystalite
Laponite[®]			
<i>Starting material</i>			
-85.2±0.1	316±7	7.7	Q ³ (0Al) ₃ , (SiO) ₃ SiOH
-94.5±0.1	263±2	79.0	Q ³ (0Al)
-97.3±0.1	188±5	13.3	Q ³ (0Al), (SiO) ₃ SiO ⁻
<i>After hydrothermal treatment in a 7.3·10⁻² M Lu(NO₃)₃·3.6H₂O solution</i>			
-90.6±0.1	258±4	27.2	δ -Na ₂ Si ₂ O ₅
-91.7±0.1	90±1	72.8	Lu ₂ Si ₂ O ₇

Table 4. ^{29}Si chemical shift, FWHM and area under the curve of the different contributions obtained from the fitting of the ^{29}Si MAS NMR spectrum of saponite and vermiculite eucatex

δ (ppm)	FWHM (Hz)	%	phase
saponite			
<i>Starting material</i>			
-85.3±0.1	55±10	0.4	Q ³ (2Al)
-90.8±0.1	210±2	35.0	Q ³ (1Al)
-95.8±0.1	220±1	64.6	Q ³ (0Al)
<i>After hydrothermal treatment in a 7.3·10⁻² M Lu(NO₃)₃·3.6H₂O solution</i>			
-72.5±0.1	146±11	2.6	Q ¹
-88.5±0.1	582±26	23.8	natrosilite (β-Na ₂ Si ₂ O ₅)
-91.7±0.2	122±1	71.4	Lu ₂ Si ₂ O ₇
-95.0±0.1	122±14	2.4	Q ³ (0Al)
vermiculite eucatex			
<i>Starting material</i>			
-84.2±0.1	679±23	10.6	Q ³ (2Al)
-88.6±0.1	590±4	40.5	Q ³ (1Al)
-93.4±0.1	549±18	8.8	Q ³ (0Al)
-99.6±0.2	2872±3	40.0	Q ⁴ (0Al), (SiO) ₄ SiOH
<i>After hydrothermal treatment in a 7.3·10⁻² M Lu(NO₃)₃·3.6H₂O solution</i>			
-76.3±0.1	818±43	4.5	Q ¹ , Q ⁰
-88.2±0.1	828±5	37.6	natrosilite (β-Na ₂ Si ₂ O ₅)
-91.4±0.2	212±1	57.9	Lu ₂ Si ₂ O ₇

544 **FIGURE CAPTIONS**

545 **Fig. 1.** XRD patterns of kanemite, pyrophyllite and talc: (a) starting material, and, (b) after
546 hydrothermal treatment at 300° C for 48 h in a $7.3 \cdot 10^{-2}$ M $\text{Lu}(\text{NO}_3)_3 \cdot 3.6\text{H}_2\text{O}$ solution.
547 *= $\text{Lu}_2\text{Si}_2\text{O}_7$ (PDF 35-0326), T=tridymite (PDF 18-1170), H= $\text{H}_2\text{Si}_2\text{O}_5$ (PDF 74-1548), and,
548 b=boehmite (PDF 76-1871).

549 **Fig. 2.** ^{29}Si MAS NMR (left) and ^1H MAS NMR (right) spectra of kanemite, pyrophyllite
550 and talc: (a) starting material, and, (b) after hydrothermal treatment at 300° C for 48 h in a
551 $7.3 \cdot 10^{-2}$ M $\text{Lu}(\text{NO}_3)_3 \cdot 3.6\text{H}_2\text{O}$ solution.

552 **Fig. 3.** XRD patterns of hectorite, Na-hectorite and Laponite®: (a) starting material, and, (b)
553 after hydrothermal treatment at 300° C for 48 h in a $7.3 \cdot 10^{-2}$ M $\text{Lu}(\text{NO}_3)_3 \cdot 3.6\text{H}_2\text{O}$ solution.
554 *= $\text{Lu}_2\text{Si}_2\text{O}_7$ (PDF 35-0326), E=enstatite (PDF 73-1937), H= $\text{H}_2\text{Si}_2\text{O}_5$ (PDF 74-1548), and,
555 C= β -cristobalite (PDF 89-3607).

556 **Fig. 4.** XRD patterns of saponite and vermiculite Eucatex: (a) starting material, and, (b)
557 after hydrothermal treatment at 300° C for 48 h in a $7.3 \cdot 10^{-2}$ M $\text{Lu}(\text{NO}_3)_3 \cdot 3.6\text{H}_2\text{O}$ solution.
558 *= $\text{Lu}_2\text{Si}_2\text{O}_7$ (PDF 35-0326), M= $\text{H}(\text{Mg}_2(\text{SiO}_4))_8$ (PDF 87-2051), O= $\text{Mg}_{10}(\text{Si}_3\text{O}_{14})(\text{OH})_4$
559 (PDF 81-544), k=kaolinite (PDF 78-1996), and, n=natrosilite (PDF 23-0529).

560 **Fig. 5.** ^{29}Si MAS NMR (left) and ^1H MAS NMR (right) spectra of hectorite, Na-hectorite
561 and Laponite®: (a) starting material, and, (b) after hydrothermal treatment at 300° C for 48
562 h in a $7.3 \cdot 10^{-2}$ M $\text{Lu}(\text{NO}_3)_3 \cdot 3.6\text{H}_2\text{O}$ solution.

563 **Fig. 6.** ^{29}Si MAS NMR (left), ^1H MAS NMR (middle) and ^{27}Al MAS NMR (right) spectra
564 of saponite and vermiculite Eucatex: (a) starting material, and, (b) after hydrothermal
565 treatment at 300° C for 48 h in a $7.3 \cdot 10^{-2}$ M $\text{Lu}(\text{NO}_3)_3 \cdot 3.6\text{H}_2\text{O}$ solution.

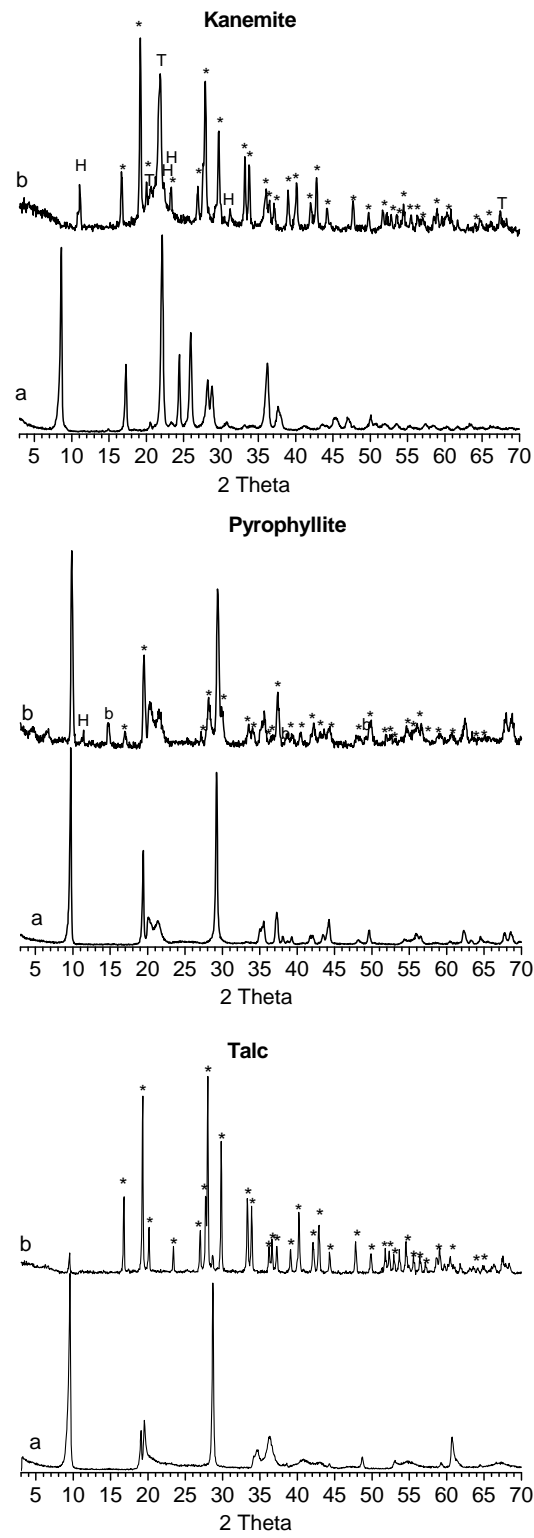
566

567

568

Fig. 1

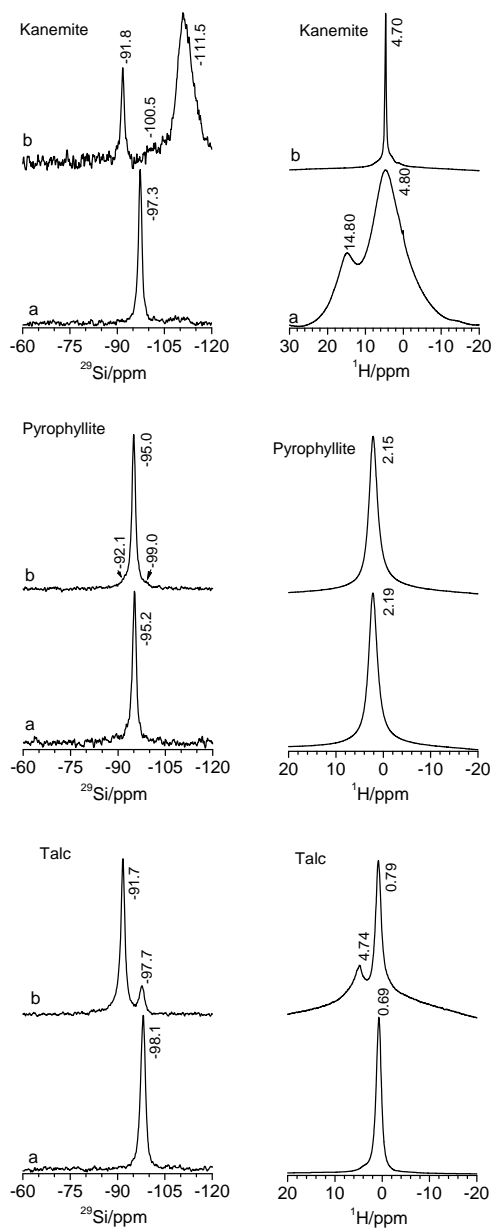
569

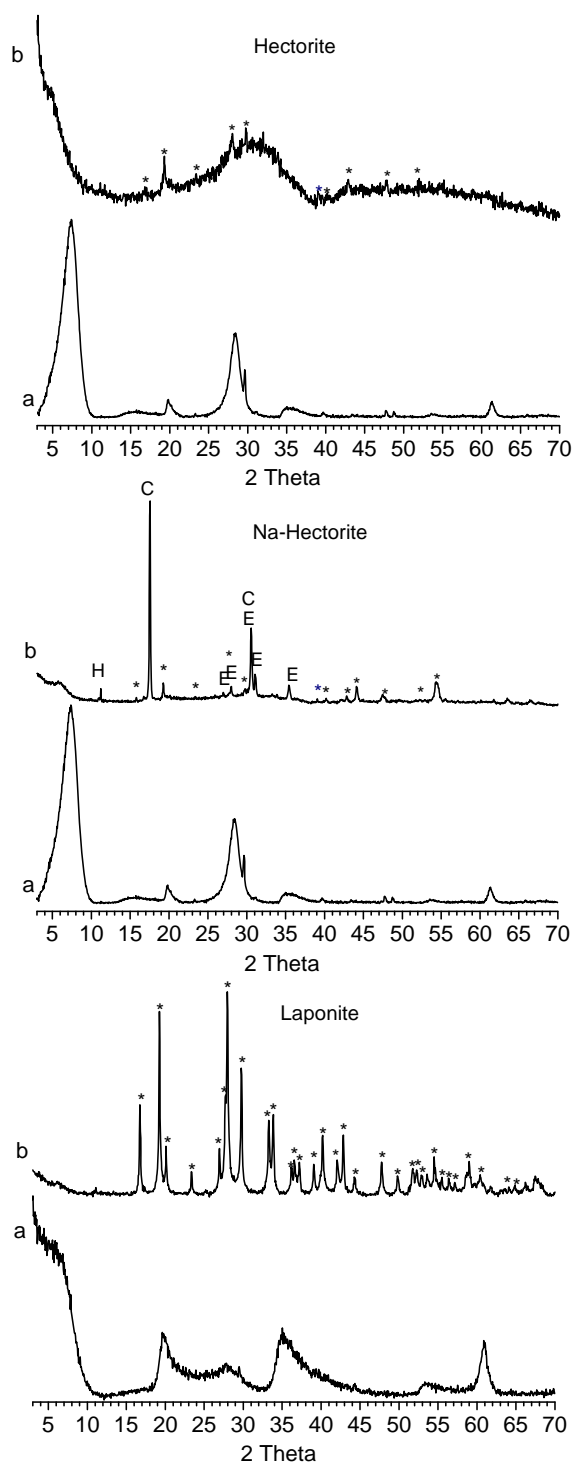


570

Fig. 2

571



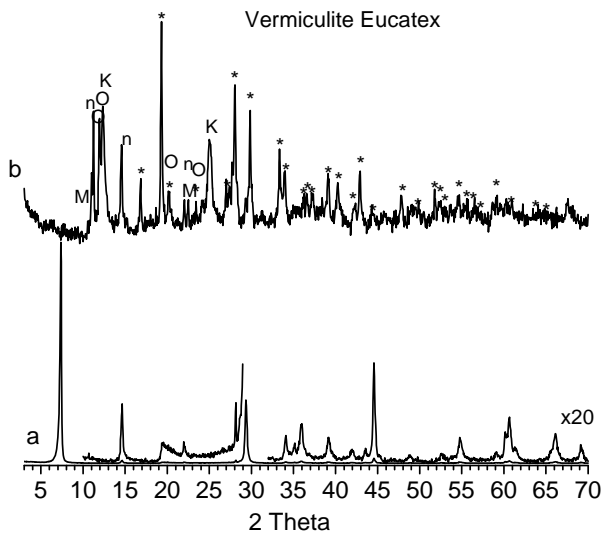
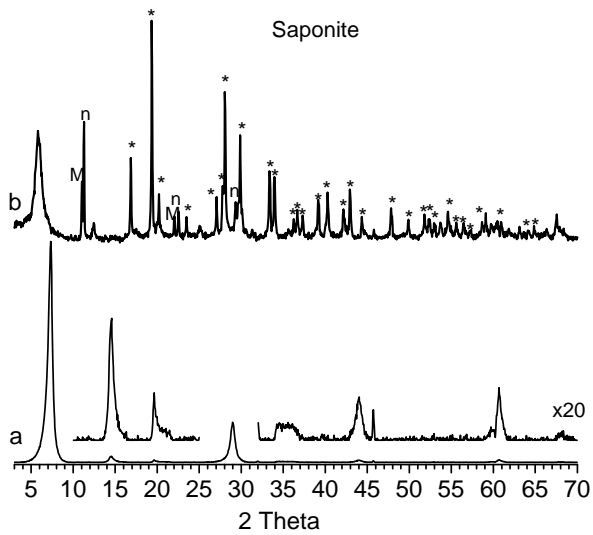


574

575

576

Fig. 4

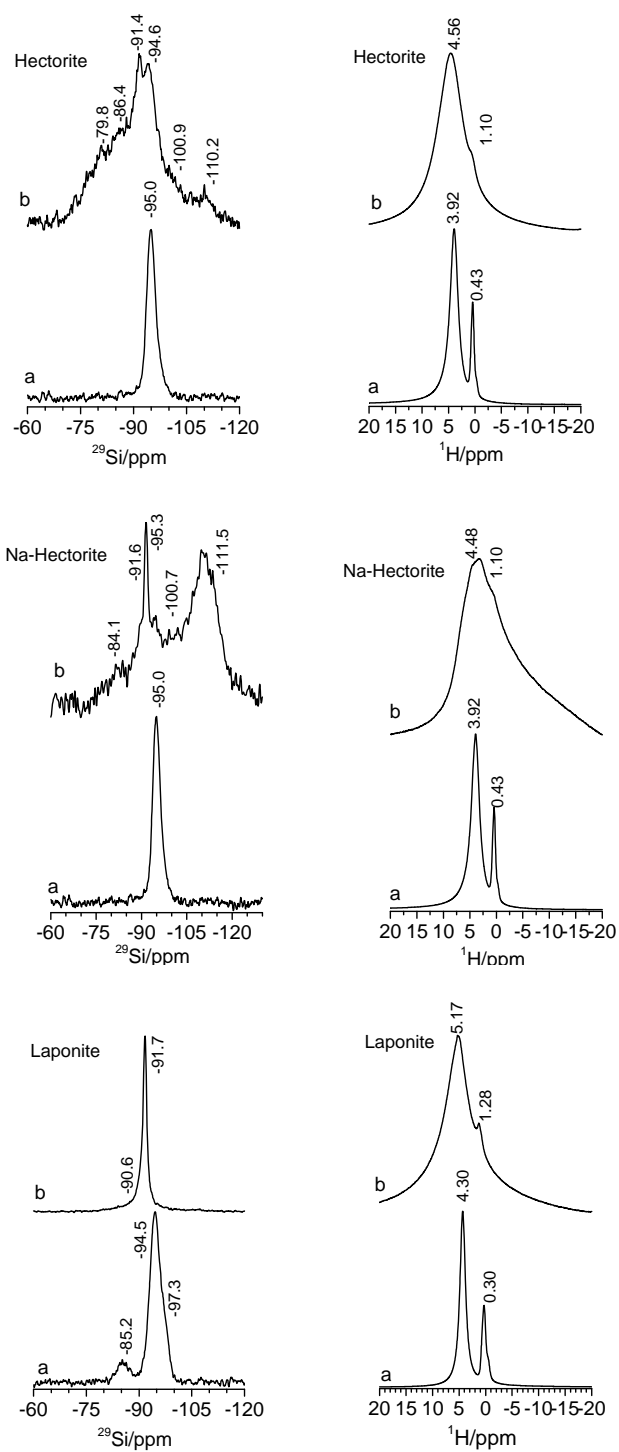


577

578

579

Fig. 5

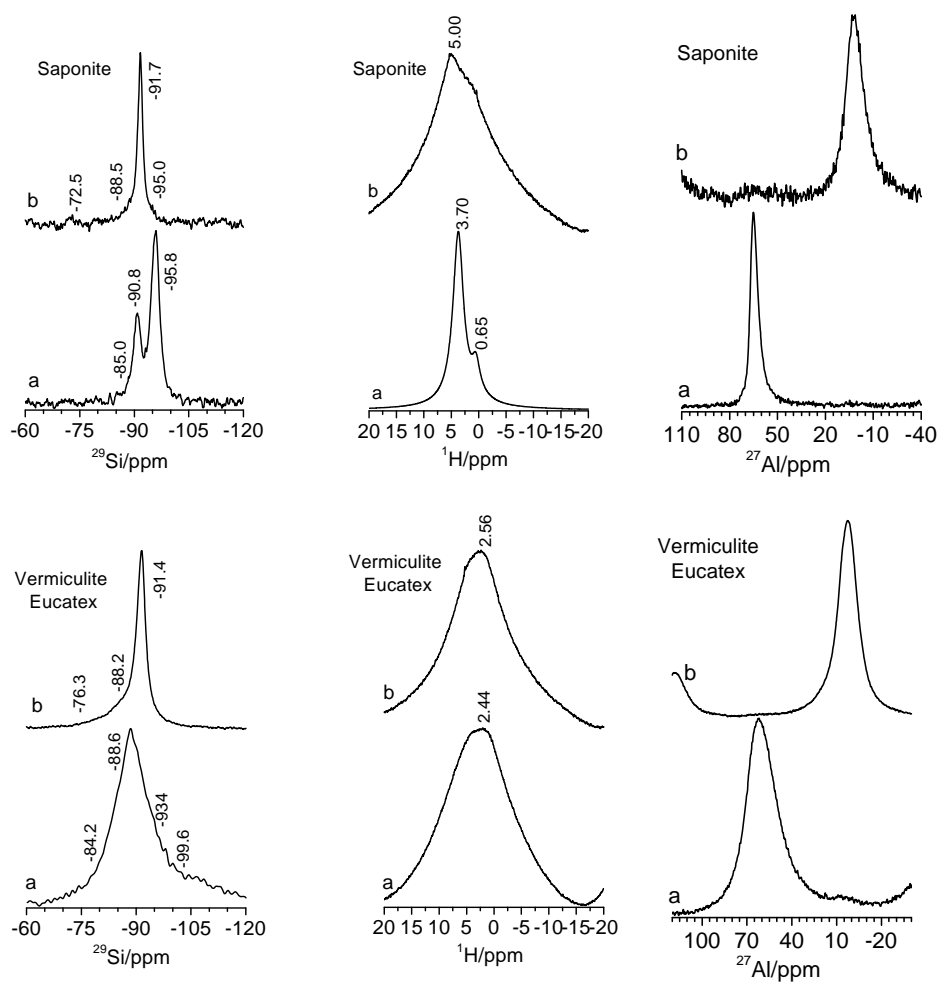


580

581

582

Fig. 6



583